

# Occurrence of a new superlattice phase across the antiferroelectric phase transition in $\text{Sr}_{1-x}\text{Ca}_x\text{TiO}_3$ ( $x = 0.30$ and $0.40$ )

Shahid Anwar<sup>1,2</sup> and N P Lalla<sup>1,3</sup>

<sup>1</sup> UGC-DAE Consortium for Scientific Research, Khandwa road, Indore 452001, India

<sup>2</sup> Central Electro Chemical Research Institute (CECRI), Karaikudi 630006, India

Received 9 May 2008, in final form 16 June 2008

Published 18 July 2008

Online at [stacks.iop.org/JPhysCM/20/325231](http://stacks.iop.org/JPhysCM/20/325231)

## Abstract

Low-temperature x-ray diffraction, low-temperature transmission electron microscopy (TEM) and dielectric permittivity studies have been carried out on  $\text{Sr}_{1-x}\text{Ca}_x\text{TiO}_3$  ( $x = 0.30$  and  $0.40$ ) ceramics across its antiferroelectric phase transition. TEM has been performed for its structural and microstructural characterizations. Together with the occurrence of the usual structural modulation along [001] of the  $P2_12_12$  (and  $Pbnm$ ), which gives rise to the  $Pbcm$  phase, clear evidences of the occurrence of a new phase, appearing as a result of structural modulation along the [110]-type direction of the  $Pbnm$ , has also been found. The temperature dependent dielectric permittivity data appears to indicate the paraelectric nature of the new phase. The coexistence of this new phase with the  $Pbcm$  phase has been attributed to  $\Delta$ -point instability, which is equally probable along any of the [100]-type directions of the basic perovskite structure. It appears that irrespective of the existing perovskite distortion, which results in  $P2_12_12$  for  $x = 0.3$  and  $Pbnm$  for  $x = 0.4$ ; the  $\Delta$ -point instability follows the cubic symmetry of the very basic perovskite.

## 1. Introduction

The high symmetry  $\text{ABO}_3$  perovskite structures undergo an antiferrodistortive (AFD) transition caused by the softening of triply degenerate  $\Gamma_{25}$ -zone-boundary phonon modes at the  $R(111)\pi/a$  of its Brillouin zone (BZ) [1, 2]. Softening of these modes corresponds to the tilting of the  $\text{BO}_6$  octahedra about its [100]-type axes. A general mode softening corresponds to condensation of a linear combination of these modes, which gives rise an AFD exhibiting a variety of structural phase transitions [1–3].  $\text{SrTiO}_3$  (ST) undergoes a  $Pm3m$  to  $I4/mcm$  phase transition at 105 K [4], which is a result of AFD occurring due to the condensation of a single such mode. Transformation of  $\text{KMnF}_3$  and  $\text{LaAlO}_3$ , at 184 K to  $Pbnm$  and at 806 K to  $R3c$ , respectively, are examples of condensation of linear combinations of two [5] and three [6] such modes. These combinations appear to give rise a variety of structures. Compositional variants of ST like  $\text{Sr}_{1-x}\text{Ca}_x\text{TiO}_3$ , (SCT) are the bench mark examples of this. Although a lot of dispute still

exists regarding identification of the correct space groups in the whole range of Ca substitution in SCT, we have recently tried to resolve a few of them for  $x = 0.20, 0.27$  and  $0.30$  [7, 8].

SCT undergoes an antiferrodistortive (AFD) transition to ferroelectric (FE) and antiferroelectric phases [3, 4]. These phase transitions have all been experimentally verified [4–8]. Through *ab initio* calculations it has been shown [3] that, generally in perovskites, two competing structural instabilities are responsible for these phase transitions. These most common instabilities are the softening of zone-center polar phonon mode and the zone-boundary phonon modes.  $\text{BaTiO}_3$  is a classical example of the first type, while  $\text{SrTiO}_3$  is the well-known example for the second type.

Ranjan *et al* [9, 10], on the basis of dielectric studies, have shown that the phase transition in SCT is paraelectric to antiferroelectric (AFE) type for  $0.18 \leq x \leq 0.40$ . The occurrence of antiferroelectric phase transition [9] is accompanied by a structural phase change to  $Pbcm$ . This AFE phase transition is identical to the one observed for  $\text{NaNbO}_3$  [11] and is related to another AFD transition resulting in modulation (doubling) of the unit cell from  $\sqrt{2}a_p \times \sqrt{2}a_p \times 2a_p$

<sup>3</sup> Author to whom any correspondence should be addressed.

(either in  $P2_12_12$  or  $Pbnm$ ) to  $\sqrt{2}a_p \times \sqrt{2}a_p \times 4a_p$  ( $Pbcm$ ) as evident from the occurrence of superlattice peaks in the x-ray diffraction (XRD) [9] and transmission electron microscopy (TEM) [12–14].  $PbZrO_3$  is another perovskite which undergoes AFE phase transition but with different unit cell dimensions  $\sqrt{2}a_p \times 2\sqrt{2}a_p \times 2a_p$  [15]. The AFE phase transitions in SCT and  $NaNbO_3$  occur due to instability at the  $\Delta$ -point of the BZ. Very few investigations have been done concerning diffraction and microstructural studies across the antiferroelectric phase transition in SCT. Recent TEM microstructural studies [14] appear to indicate an independent character of the  $\Delta$ -point instability with respect to the  $\Gamma_{25}$ -zone-boundary phonon mode instability. This gives a hint that other types of superlattice phases may also appear due to instability of the  $\Delta$ -points in the BZ related to the cubic symmetry. No occurrences of such an observation have yet been reported.

Therefore, keeping the above in mind, low-temperature (LT) as well as room-temperature (RT) TEM investigations were carried out on well-characterized  $Sr_{1-x}Ca_xTiO_3$  ceramics with  $x = 0.3$  and  $0.4$ . Here we present the results, which clearly bring out the occurrence of a new type of superlattice ordering across the AFE phase transition in SCT. Together with this we also discuss the effect of disorder, probably due to oxygen vacancy, on the nature of the first-order antiferroelectric phase transition in SCT40.

## 2. Experimental details

Well sintered (at  $1300^\circ\text{C}$  for 24 h) ceramic pellets of  $Sr_{1-x}Ca_xTiO_3$  with  $x = 0.30$  and  $0.40$  (here after termed as SCT30 and SCT40), were prepared through solid-state reaction and semi-wet routes, using  $SrCO_3$ ,  $CaCO_3$ ,  $SrNO_3$ ,  $CaNO_3$  and  $TiO_2$ . Details of the solid-state and semi-wet routes are given in our previous reports [7, 14]. The sintered pellets were then crushed and ground to fine powders. Keeping in mind the possible effects of oxygenation, which are usually expected for all perovskite oxides, two sets of pellets were prepared out of these powders of SCT30 and SCT40 ceramic. For the first set of pellets the same as-crushed powder was used and for the second set the powders were first annealed in a pure (99.99%) oxygen atmosphere at  $950^\circ\text{C}$  for 24 h. The pellets were then finally sintered at  $1350^\circ\text{C}$  for 12 h. To check the quality of the final sintered ceramic samples dielectric permittivity measurements were carried out on them from 380 down to 100 K. The samples were subjected to RT and LT XRD and TEM characterizations. TEM samples were prepared by cutting 3 mm disks from the corresponding pellets. The disks were then mechanically thinned to  $\sim 70\ \mu\text{m}$  and subsequently dimpled to  $\sim 20\ \mu\text{m}$ . The dimpled disk was then made electron transparent by ion-beam polishing, employing twin argon ion-guns operating at 3.3 kV and set at grazing incidence of  $3^\circ$ . A  $LN_2$  based LT-XRD setup and a double-tilt  $LN_2$  based LT-TEM holder (636MA-Gatan), with tilt limits of  $\alpha = \pm 45^\circ$  and  $\beta = \pm 25^\circ$ , were used for the LT structural phase transformation studies.

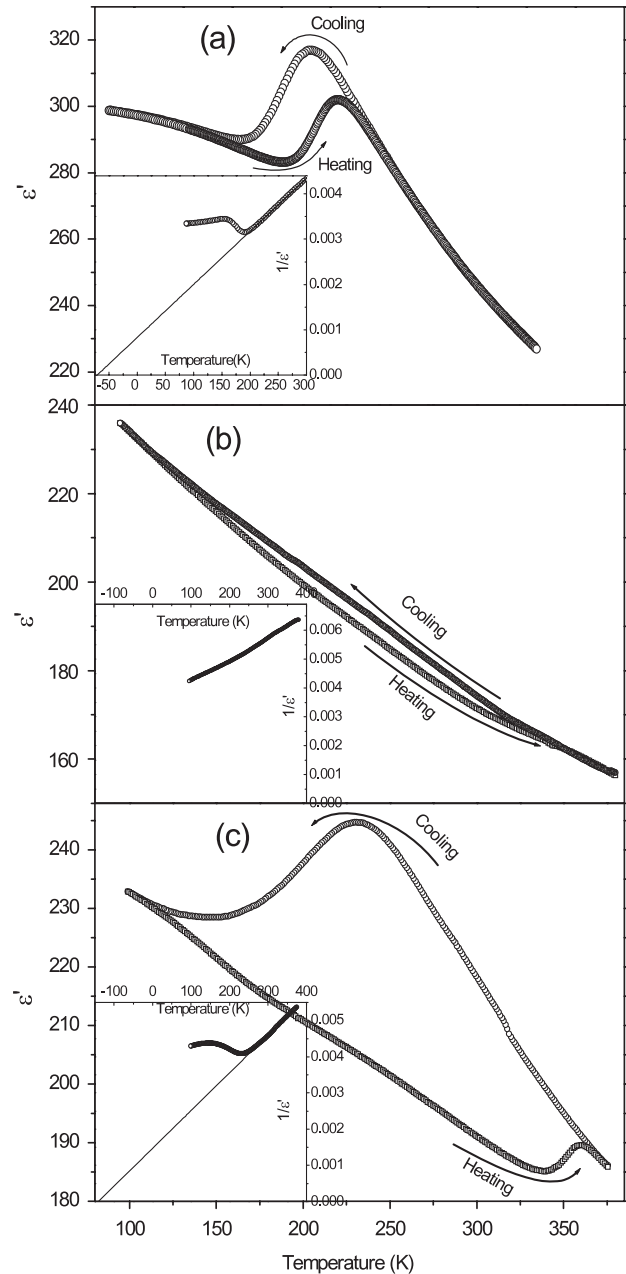


**Figure 1.** Temperature variation of the real part of the dielectric permittivity ( $\epsilon'$ ) for (a) un-oxygenated SCT30, (b) un-oxygenated SCT40 and (c) oxygenated SCT40. It should be noted that oxygenation has no appreciable effect on the  $\epsilon'$ - $T$  behavior of SCT30. Whereas for SCT40 oxygenation sharpens the transition. The occurrence of well-defined thermal hysteresis with sharp transitions in ( $\epsilon'$ - $T$ ) shows the formation of high quality SCT30 and SCT40 ceramics after oxygenation.

## 3. Results and discussion

### 3.1. Dielectric studies

The quality of the samples was also verified by conducting dielectric measurements on them. A good quality sample of SCT is supposed to show a sharp antiferroelectric phase transition, which is a characteristic of these ceramics. Figure 1 depicts the variation of the real part of the dielectric

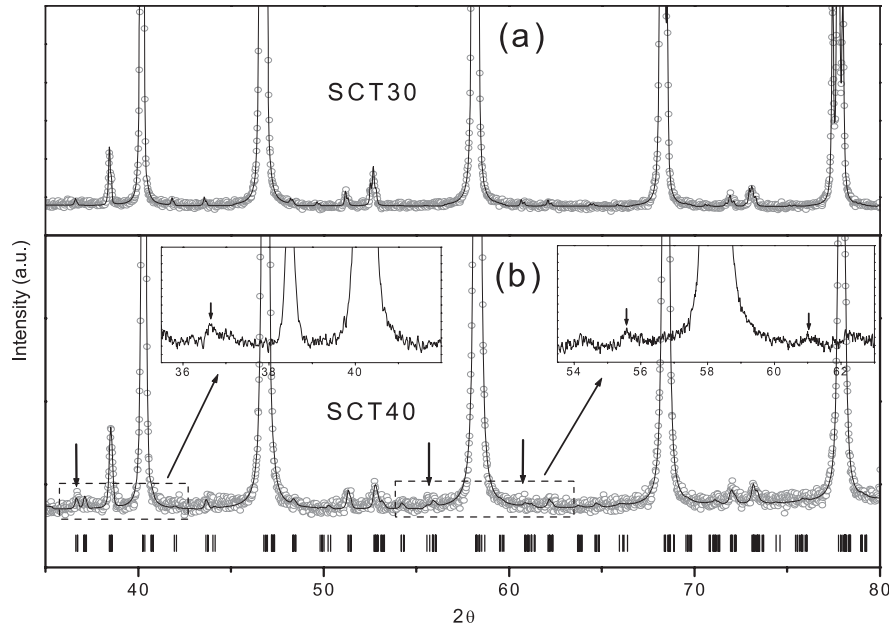


**Figure 2.** Rietveld refined room-temperature XRD data of (a) SCT30 and (b) SCT40 ceramics with  $P2_12_12$  and  $Pbcm$  space groups. Insets show the enlarged view of the superlattice peaks due to SCT40. It should be noted that there was no appreciable structural change on oxygenation.

permittivity ( $\epsilon'$ ) as a function of temperature for (a) SCT30 (b) un-oxygenated SCT40 and (c) oxygenated SCT40 samples. Since no appreciable difference was observed between the  $\epsilon'-T$  behaviors of un-oxygenated SCT30 and oxygenated SCT30, we have only presented here the  $\epsilon'-T$  data corresponding to the un-oxygenated SCT30. In fact during a detailed dielectric study carried out on a series of SCT ceramics, containing 20–40% calcium, it has been shown that only those SCT ceramics which contain more than 30% Ca show a drastic change in their  $\epsilon'-T$  behavior after oxygenation [16]. It is evident from the negative values of the Curie temperatures, as determined from the Curie–Weiss plots shown in the insets of figure 1, that the sharp maxima in  $\epsilon'-T$  at 198 K for SCT30 and 230 K for SCT40 correspond to an antiferroelectric phase transition. It can be seen that the characteristics of the measured thermal hysteresis are quite different for the oxygenated and un-oxygenated SCT40 samples. The transition width is much wider for the un-oxygenated SCT40 sample. After oxygenation the transition widths have become much sharper. This indicates that the observed broadening originates from the oxygen deficiency in SCT40. However, no such appreciable change was observed for SCT30. In the following we will discuss the effect of broadening of the phase transition and the structural phase coexistence.

### 3.2. X-ray diffraction studies

Figure 2 shows the room-temperature powder XRD patterns of (a) SCT30 and (b) SCT40 ceramics. The XRD pattern of SCT30 was Rietveld refined using  $P2_12_12$  space group [7] with a goodness of fit of  $\sim 2.72$ . The extra superlattice peaks, as marked by arrows in the XRD pattern of SCT40, are

indexable using an orthorhombic cell with lattice parameters  $\sqrt{2}a_p \times \sqrt{2}a_p \times 4a_p$ . In the literature [9] these are attributed to AFE ordering resulting in  $Pbcm$  phase. We, too, could successfully refine this based on the reported structural parameters for the  $Pbcm$  phase. Absence of any unaccounted peak in both cases shows the formation of single phase ceramics. An enlarged view of the superlattice peaks is shown in the corresponding insets of figure 2(b). Here we would like to emphasize that oxygenation did not have any effect on the structure (change in space group). The superlattice peaks were equally present in oxygenated and un-oxygenated SCT40 samples.

Here we would like to emphasize that since powder XRD is a one-dimensional aggregation of three-dimensional (3D) crystallographic information, accurate identification of the coexistence of structurally close phases like  $P2_12_12$ ,  $Pbnm$  and  $Pbcm$ , which differ only in the presence (or absence) of some very weak reflections, may not be possible using lab. XRD data. Therefore for an accurate structural characterization TEM investigation, which is capable of providing 3D crystallographic information without missing even the weakest reflection, has necessarily been carried out on ion-polished samples of SCT30 and SCT40.

### 3.3. Low-temperature structural studies on SCT30

As revealed by the dielectric measurement, SCT30 undergoes a paraelectric ( $P2_12_12$ ) to antiferroelectric ( $Pbcm$ ) phase transformation at 198 K. During this phase transition the electric dipole moments gets aligned antiparallel along the  $c$ -axis [9] causing a doubling of the  $c$ -parameter of the parent lattice. To check the bulk presence of the  $Pbcm$  phase, low-temperature (LT) XRD was carried out. Figure 3 shows the

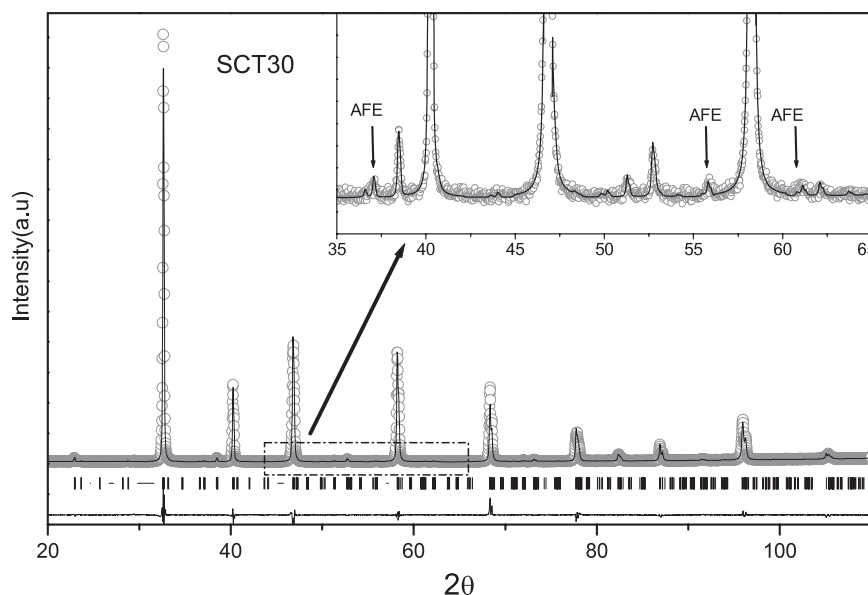


Figure 3. Rietveld refined low-temperature XRD data of SCT30, with space group *Pbcm*.

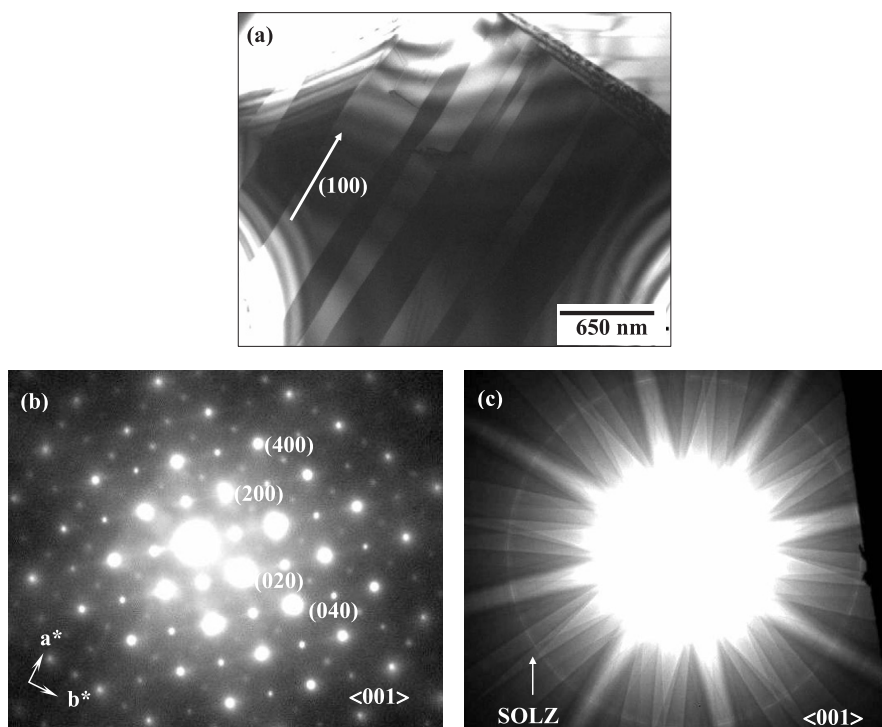
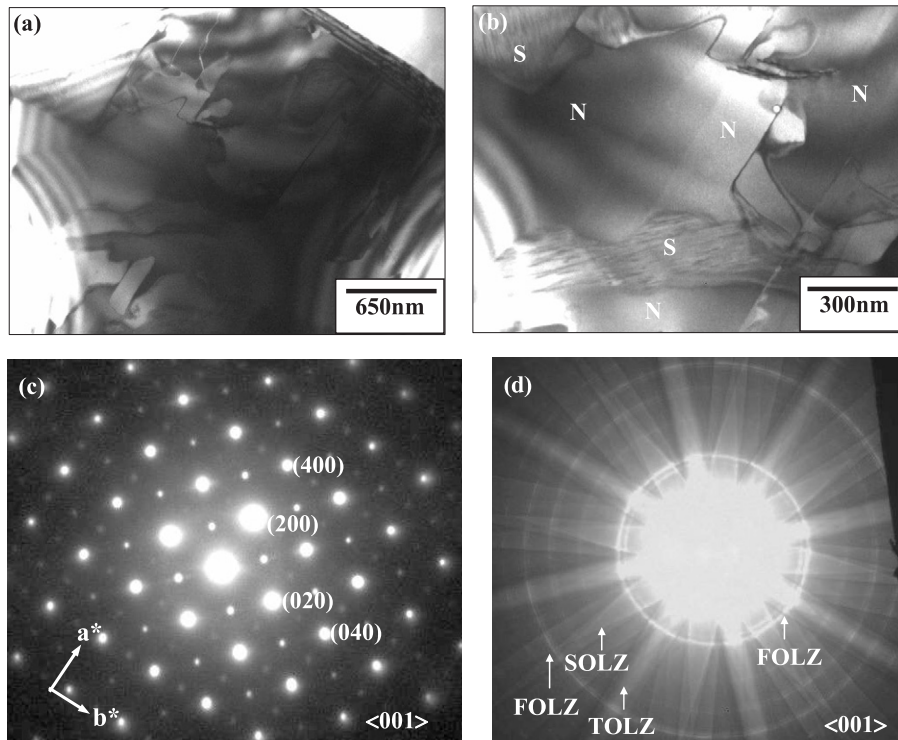


Figure 4. (a) Room-temperature electron micrograph showing twin band like contrast in oxygenated SCT30. (b) and (c) show SAD and wide-angle CBED patterns taken along  $\langle 001 \rangle$  zone from the twin bands. The bands were found to be mirror related twins of the  $P2_12_12$  phase about  $\langle 100 \rangle$  plane.

LT-XRD data of SCT30, which has been Rietveld refined using the *Pbcm* space group. The superlattice peaks, occurring due to doubling of the cell parameter during antiferroelectric ordering, are marked by arrows. To properly identify the antiferroelectric ordering and also to characterize the related microstructural changes RT and LT-TEM investigations on SCT30 were carried out on ion-milled samples. Figure 4(a) represents a typical electron micrograph of SCT30 recorded

at RT. This exhibits a twin band contrast. To determine the correct phase (space group) of these twins, SAD and wide-angle CBED patterns were taken from the consecutive bands. The consecutive twin bands were found to give similar SAD and CBED patterns. Representative SAD and CBED patterns are shown in figures 4(b) and (c) respectively. Based on the method given in our previous studies [7, 8], the twins were characterized to be an orthorhombic distorted perovskite



**Figure 5.** (a) and (b) Low-temperature (106 K) electron micrographs showing the *Pbcm* domains, which have formed after random nucleation of *Pbcm* phase among the parallel twin bands of oxygenated SCT30. Two types of regions marked N and S can be seen in (b). (c) and (d) are respectively SAD and wide-angle CBED patterns taken along  $\langle 001 \rangle$  zone from the N-type region. These patterns confirm the *Pbcm* phase of the N-type regions.

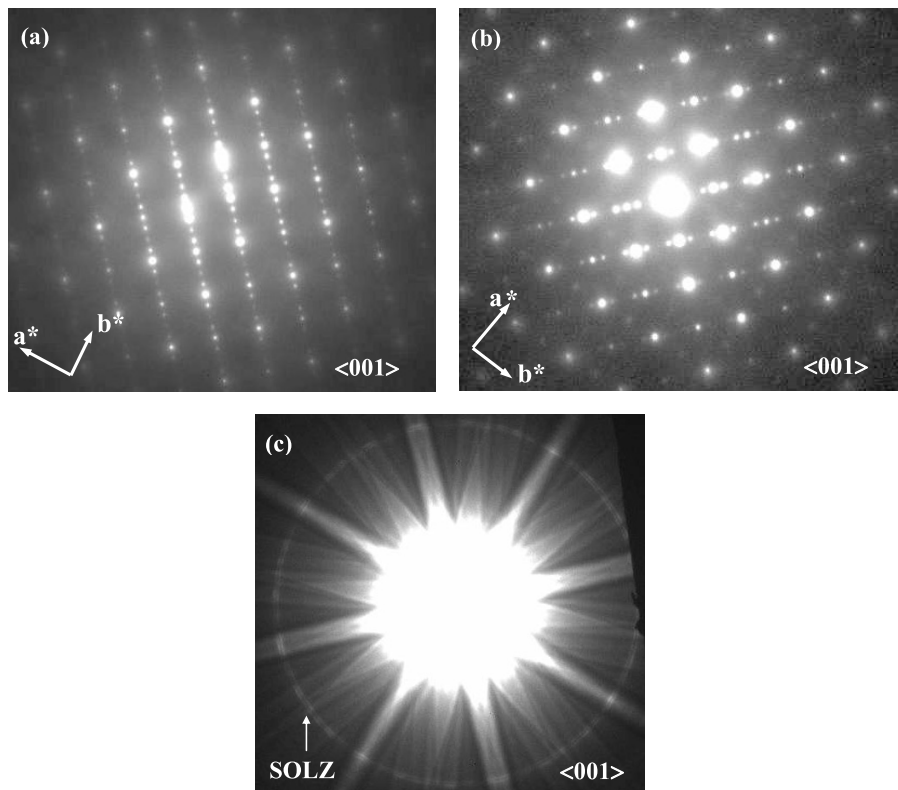


**Figure 6.** (a), (b)  $\langle 001 \rangle$  zone SAD patterns taken at 106 K from regions marked S in figure 5(a). It shows strong four-fold modulation along  $[110]$  of  $P2_12_12$ . (c) A typical wide-angle CBED taken along the  $\langle 001 \rangle$  zone of the same S-type domain of oxygenated SCT30.

phase with space group  $P2_12_12$  and lattice parameters  $a = 5.4818 \text{ \AA}$ ,  $b = 5.4844 \text{ \AA}$ ,  $c = 7.7878 \text{ \AA}$  [8]. Careful measurements repeated on several pairs of SADs taken from the neighboring bands, revealed that the observed bands are mirror related with (100) as the twin plane (the interface of the bands). Details of the twin analysis will be published elsewhere. The entire twin bands are found to be oriented along the [001] direction. Here we would also like to emphasize that unlike the powder SCT30 [7, 8], the bulk SCT30 is found to be single  $P2_12_12$  phase only. To study the microstructural changes and other related structural features, occurring across the AFE phase transition, low-temperature TEM (LT-TEM) was carried out at temperatures between 106 and 300 K. Figure 5(a) shows an electron micrograph recorded at 106 K from the same grain as shown in figure 4(a). It can be noticed that below the AFE phase transition at 180 K, the microstructural features have completely changed. The twin band like contrast observed prior to the transition has changed to a randomly broken domain structure. Observation at higher magnification shows two types of regions, which have been marked here as N and S, see figure 5 (b). The N-type regions, which are in abundance, have smooth contrast whereas the S-type regions, which are fewer, show some irregular fine lamellar contrast. The fine lamellar contrast was found to have two mutually perpendicular orientations. The S-type microstructure was found in some limited grains only. Figures 5(c) and (d) exhibit typical SAD and CBED patterns taken from N-type regions. As compared to figure 4(b), although the SAD look identical the wide-angle CBED is completely different from that of the RT ones. The generally invisible FOLZ corresponding to (001) period of  $P2_12_12$  has appeared with two extra HOLZ rings. The change in periodicity along [001] was measured using the HOLZ ring diameters. The smallest HOLZ ring was found to correspond to  $15.5 \text{ \AA}$ . The periods corresponding to other HOLZs were found to be integrally related with the period of the smallest HOLZ. Thus the N-type regions were found to be orthorhombic phase with lattice parameters  $\sqrt{2}a_p \times \sqrt{2}a_p \times 4a_p$ , which belongs to the reported AFE [9–11]  $Pbcm$  phase in SCT. The S-type regions, were found to give SAD patterns as shown in figures 6(a) and (b). Figure 6(c) depicts a representative wide-angle CBED pattern from the S-type regions. The occurrence of strong modulation along the [110] direction in the [001] zone patterns in figures 6(a) and (b) and the absence of extra HOLZ rings in the CBED pattern shown in figure 6(c), as compared to the CBED pattern shown in figure 5(d), can be clearly noticed. Keeping in mind the RT microstructure of the paraelectric phase, which has only [001] oriented twin bands, the above-mentioned features in SAD and CBED taken from the S-type regions are quite unusual. According to earlier reports [9–11] the occurrence of the  $Pbcm$  phase in the AFE states of SCT and  $\text{NaNbO}_3$  is not expected to cause any modulation in the  $a^*b^*$  plane at all. It will modulate (doubly) only the  $c$ -direction. Therefore the regions marked S in the micrograph shown in figure 5(b) represent a new type of superlattice phase occurring across the PE to AFE phase transition boundary in SCT30. The usual  $Pbcm$  phase coexists with this. This unusual modulation was found to occur only

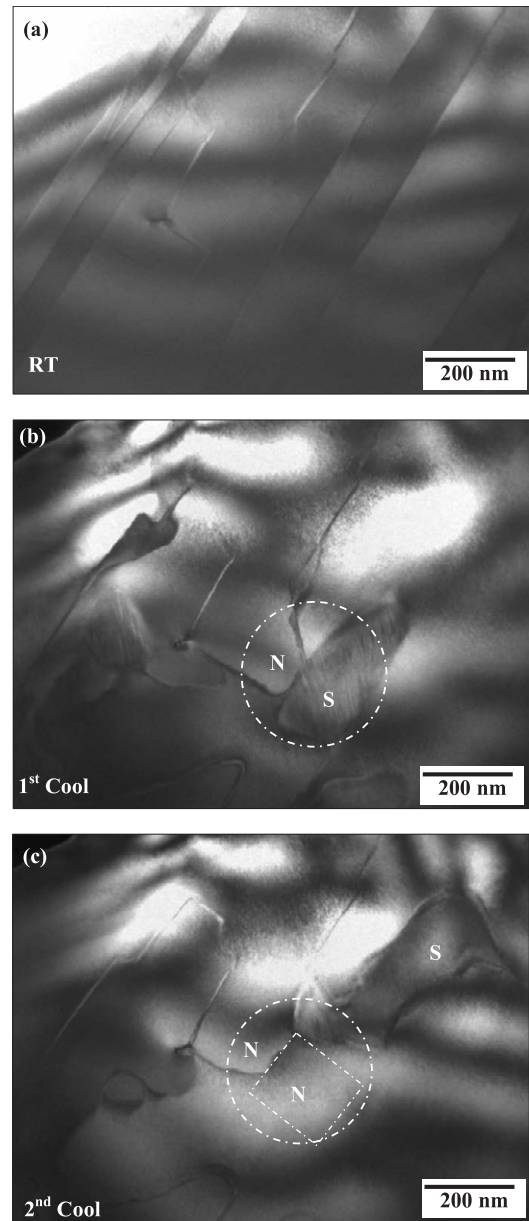


**Figure 7.** TEM micrographs of the same region of oxygenated SCT30 taken at (a) room temperature, (b) low temperature (LT), 106 K, during the 1st cooling, and (c) LT during the 2nd cooling. A comparison of (b) and (c) clearly shows the randomness of the nucleation and growth of the  $Pbcm$  phase during the AFE transition. The inter-convertibility of N- and S-type regions can be clearly seen in the dashed rectangular region.

along two mutually perpendicular directions [110] and  $[\bar{1}10]$  of the  $P2_12_12$  phase.

Figures 7(a)–(c) show a comparison of electron micrographs taken at (a) RT, (b) after the very first cooling and (c) after the second cooling. Both the low-temperature micrographs have been taken at 106 K. The 2nd cool LT-micrograph has been taken after heating the sample to RT after its first cooling and then again lowering the temperature for the 2nd cool down to 106 K. The difference in the first cool LT-micrograph with respect to that of the RT one, is due to random nucleation and growth. This is to be expected during any first-order

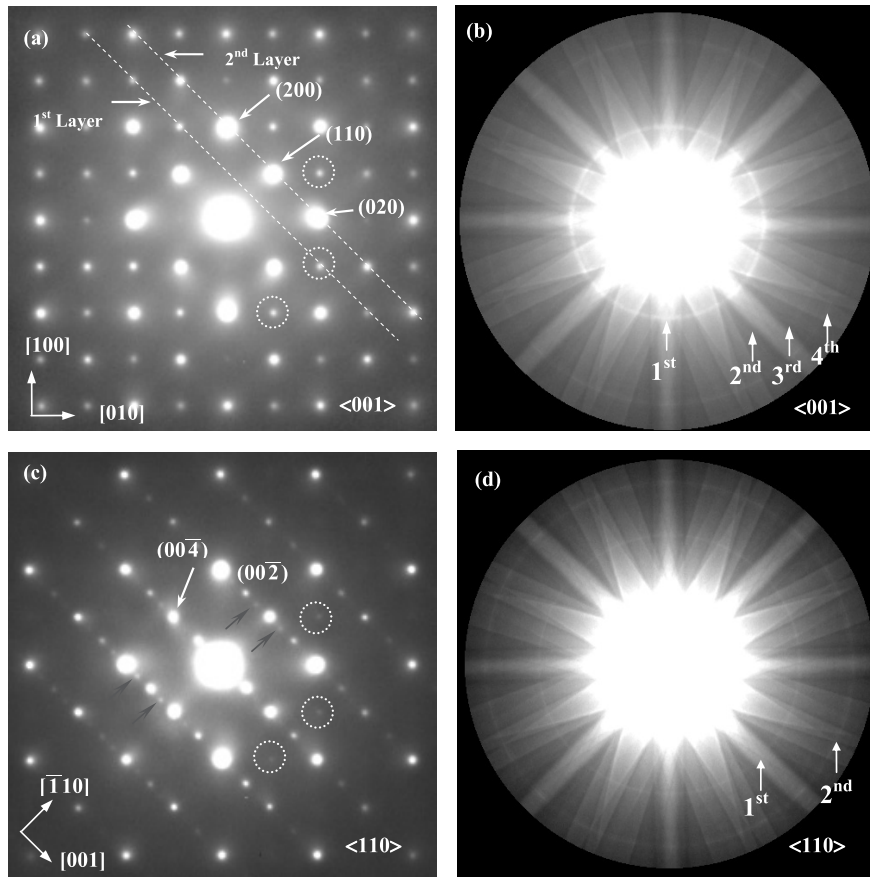


**Figure 8.** SAD and CBED patterns (a), (b) taken along  $[001]$  and (c), (d) along  $[110]$  zones of the  $Pbcm$  phase in the un-oxygenated SCT40. The occurrence of the FOLZ ring as well as the superlattice spots, as indicated by arrows, exhibit the cell doubling corresponding to  $15.5 \text{ \AA}$ .

phase transition. The 1st and 2nd cool LT micrographs taken at the same temperature are different and include some important feature. This can be seen by comparing the circled regions in the two LT micrographs. It can be seen that some part of the S-type region has been converted into an N-type region during the 2nd cool. This is indicated by the dashed rectangle. The conversion of an S-type region into an N-type asserts that the observed new superlattice phase is not entirely the outcome of some compositional inhomogeneity in the grains. The inter-convertibility of S and N-type regions itself proves this.

As already mentioned, the SAD and CBED in figure 5 correspond to the AFE  $Pbcm$  phase with lattice parameter  $\sqrt{2}a_p \times \sqrt{2}a_p \times 4a_p$ . This AFE phase transition is due to the  $\Delta$ -point instability of the basic perovskite BZ [9]. The occurrence of the unusual superlattice ordering along  $[110]$  and  $[\bar{1}10]$  of the room-temperature  $P2_12_12$  phase also appears to be related to similar  $\Delta$ -point instability of the BZ.

### 3.4. TEM studies on un-oxygenated SCT40

**3.4.1. Superlattice reflections occurring at room temperature from the  $Pbcm$  phase in un-oxygenated SCT40.** Figures 8(a) and (c) present SAD patterns taken from neighboring domains of un-oxygenated SCT40 and (b) and (d) present CBED patterns corresponding to the SADs in 8(a) and (c). Figure 8(a) is a typical ZOLZ pattern seen along the major axis  $[001]$

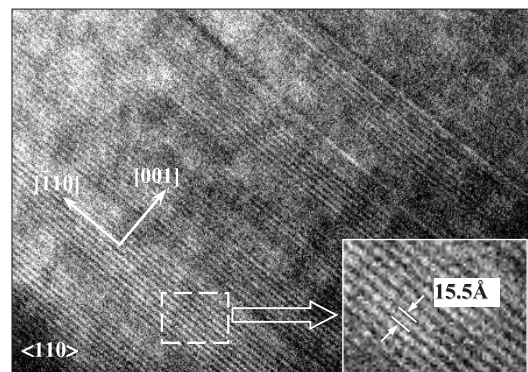


**Figure 9.** Electron micrograph of un-oxygenated SCT40 showing  $15.5 \text{ \AA}$  lattice fringes corresponding to cell doubling along the  $c$ -axis of the  $Pbnm$  phase.

of  $Pbnm$  and  $Pbcm$ . It should be noted that the spots with indices  $\{h00\}$  and  $\{0k0\}$  with  $h$  and  $k$  odd, are forbidden both in  $Pbnm$  and  $Pbcm$  but appear as a result of double diffraction [7]. The FOLZ ring, as marked by 1st in the CBED pattern of figure 8(b), measures a  $15.5 \text{ \AA}$  periodicity in direct space and hence corresponds to the  $[001]$  reciprocal layer of the  $Pbcm$  phase. This is double the  $c$ -parameter ( $7.78 \text{ \AA}$ ) of the  $Pbnm$  phase. It should be noted that the cell doubling occurs during the paraelectric ( $Pbnm$ ) to antiferroelectric

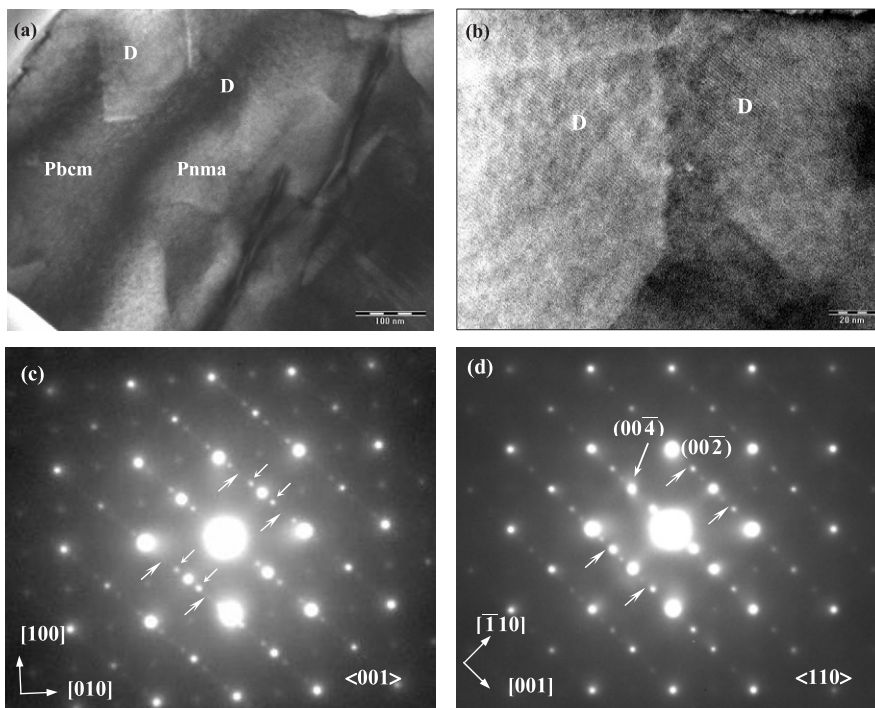


**Figure 10.** Electron micrograph of un-oxygenated SCT40 showing the presence of *Pbnm* and *Pbcm* phases. Domains marked D show a new type of superlattice ordering in the SAD pattern shown in (c) and the lattice fringes (b) corresponding to domain D. The SAD in (d) shows a *Pbcm* ordering. A close comparison of (c) and (d) clearly reveals the difference; compare the intensity of spots indicated by arrows.

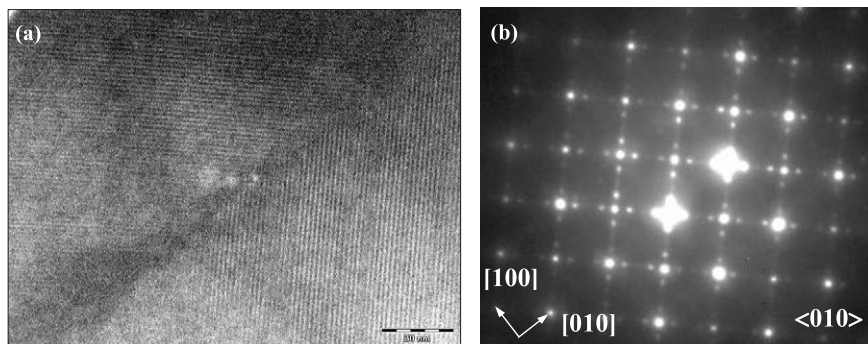


**Figure 11.** (a) Electron micrograph of un-oxygenated SCT40 showing lattice fringes from twin domains. (b) The corresponding SAD pattern.

(AFE) (*Pbcm*) phase transition [17, 18]. The other HOLZ rings, as indicated by arrows, are relatively weak. The direct evidence of cell doubling along [001] can be found in the [110] zone SAD pattern shown in figure 8(c) and the corresponding direct lattice-resolution micrograph as shown in figure 9. The presence of extra spots in the middle of the fundamental spots of *Pbnm* phase (as indicated by black arrows in figure 8(c)), and the corresponding 15.5 Å lattice fringes in figure 9, indicate the cell doubling of the antiferroelectric phase. The HOLZ rings in the  $\langle 110 \rangle$ -zone CBEDs marked as 1st and 2nd in figure 8(d) correspond to FOLZ and SOLZ. These rings appear as a result of the intersection of the Ewald-sphere with the reciprocal lattice layers indicated as 1st layer and 2nd layer in the ZOLZ given in figure 8(a). These superlattice reflections appear as a result of the doubling of the *c*-parameter of the paraelectric (*Pbnm*) phase. This has been attributed to

the effect of antiparallel displacement of  $\text{Ti}^{4+}$  and  $\text{Sr}^{2+}/\text{Ca}^{2+}$  ions within the orthorhombic cell of the paraelectric phase. Such an antiferroelectric phase transition was first observed in  $\text{NaNbO}_3$  [11] and later identified for SCT by Ranjan *et al* [9].

3.4.2. Occurrence of the new superlattice phase at room temperature in un-oxygenated SCT40. A new type of superlattice phase as shown in figure 6 has also been observed for SCT40, coexisting with the *Pbnm* and *Pbcm* phases. Figure 10(a) shows an electron micrograph of SCT40. Different domains are clearly visible. Domains marked *Pbnm* and *Pbcm* exhibit SAD and CBED patterns identical to those shown in figure 8 confirming the presence of *Pbnm* and *Pbcm* phases in the respective domains [14]. However, the domains marked D give a completely new type of SAD as shown in figure 10(c). The lattice-resolution micrograph corresponding

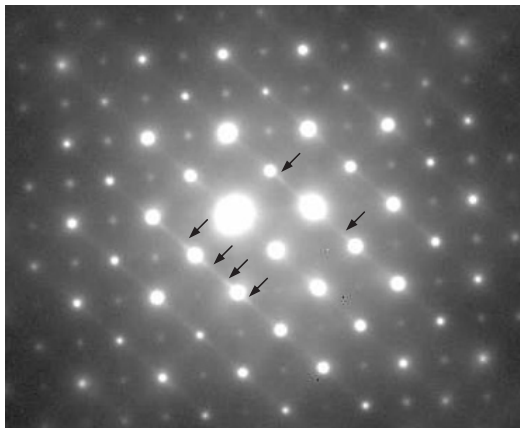


**Figure 12.** The SAD pattern from D-type domains, see figure 10 (b), taken at 360 K. The occurrence of diffuse superlattice spots, as shown by arrows, indicate the transformation of the new phase at high temperatures.

to domains D is shown in figure 10(b). The lattice fringes correspond to 15.5 Å. Superlattice spots, occurring along the [110]-type direction of the *Pbnm*, around the intense reflections, are marked by small arrows in figure 10(c). Here we would sincerely point out that it is quite likely that one may confuse this new superlattice ordering with the one seen for the *Pbcm* phase, because both have the same period. But this new superlattice ordering is different and is expected to give rise to a different crystal structure than *Pbcm*. To clarify this point, the corresponding SAD pattern of the *Pbcm* phase, which is already shown is figure 8(c), has once again been presented here as figure 10(d), for easier comparison. The spots marked by large arrows in figure 10(d) are very weak in figure 10(c). Similarly the superlattice spots, which are marked by small arrows in figure 10(c) are much more intense than those of figure 10(d). Thus it can be realized that the two patterns have a basically different look. This comparison clarifies that the pattern shown in figure 10(c), corresponds to a different type of superlattice phase other than the *Pbcm* phase being present in domains marked D. While *Pbnm* transforms to *Pbcm*, cell doubling occurs along [001] direction of the *Pbnm*, but the observed new superlattice phase appears as a result of an ordering along [110] of the *Pbnm* phase. In other

grains the D-type domains have also been observed as twin domains. Figure 11 exhibits (a) a lattice-resolution micrograph and (b) the corresponding SAD pattern from such a twin related domains of the new superlattice phase.

To check the stability of this new phase in SCT40 we heated the sample above RT to 375 K. It was observed that the superlattice spots get slowly diffused and finally vanish at  $\sim 375$  K, see figure 12. The new phase was also cooled below RT down to 100 K. It was found that the newly observed superlattice phase persists down to 100 K, see figures 13(a) and (b). Figure 13 shows (a) a lattice-resolution micrograph and the corresponding (b) SAD pattern taken at 100 K. They are identical to the one observed at room temperature.

While exploring SCT40 at 100 K, a few regions exhibiting superlattice modulation along two mutually perpendicular directions were encountered. The corresponding lattice-resolution micrograph and SAD pattern are shown in figures 14(a) and (b). The micrograph contains mutually perpendicular two-dimensional lattice fringes. This particular observation unequivocally proves the existence of a superlattice ordering other than the one observed for the *Pbcm* phase.

### 3.5. TEM studies on oxygenated SCT40

Figure 15(a) shows an electron micrograph of a grain of oxygenated SCT40 sample, to which the  $\epsilon'-T$  curve, shown in figure 1(c), corresponds. This also shows a similar domain structure to that observed in figure 10(a). The [001] zone SAD and low-angle CBED shown in figures 15(b), and (c) have been taken from the domain marked 'A'. Wide-angle CBED along the [001] zone were also taken from various such thin grains. However, even after repeated exploration we could not find a grain exhibiting [001] zone CBED having a HOLZ ring corresponding to 15.5 Å, like the ones shown in figures 5(d) and 8(b), which should be present if the grain belongs to *Pbcm* phase. This indicates either a little presence or perhaps the complete absence of the *Pbcm* phase at room temperature in the oxygenated SCT40 sample. The occurrence of mirrors  $m_1$  and  $m_2$  in the low-angle CBED in figure 15(c), as indicated by 'dashed' line along the GM-lines in the forbidden disks of type ( $h00$ ) and ( $0k0$ ),  $h$  and  $k$  being odd, occurring respectively along the [100] and [010] directions, confirm the *Pbnm* phase.

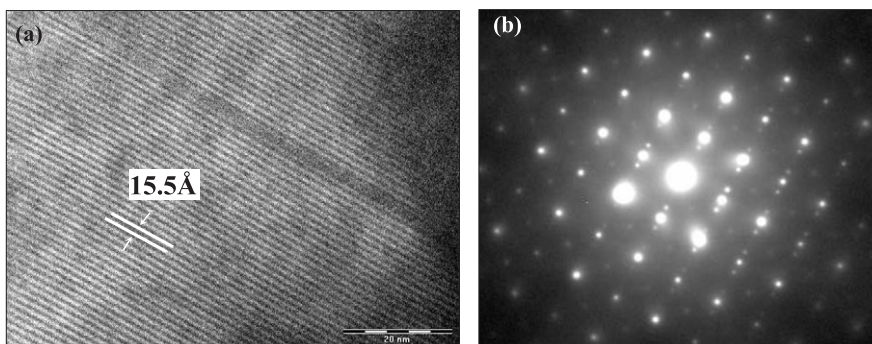


**Figure 13.** (a) Lattice-resolution electron micrograph and the corresponding (b) SAD pattern observed for the new superlattice phase in un-oxygenated SCT40, at 100 K. Please note that the SAD pattern has deliberately been rotated by 90° to match with the direction of the superlattice modulation.

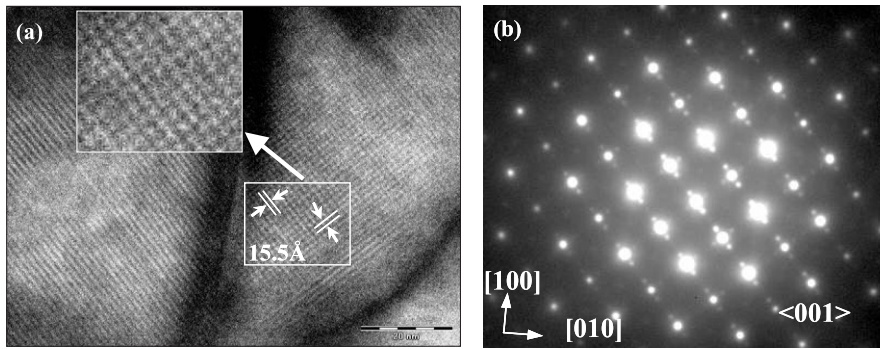


**Figure 14.** (a) Lattice-resolution electron micrograph and the corresponding (b) SAD pattern in un-oxygenated SCT40 showing the occurrence of two-dimensional ordering (see inset) of period 15.5 Å, in the same domain. This unequivocally proves the occurrence of a new type of ordering other than the *Pbcm*.

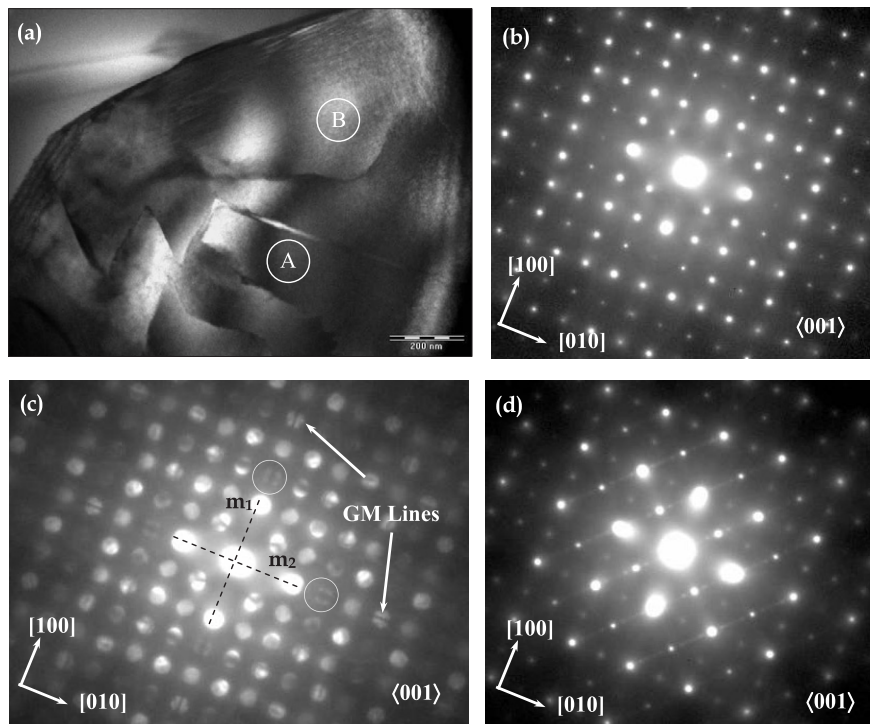


**Figure 15.** (a) Electron micrograph of *Pbnm* domains in a grain of oxygenated SCT40, (b) and (c) SAD and CBED patterns taken from region marked 'A' and (d) SAD from region marked 'B'. SAD from region 'B' shows the occurrence of the new superlattice phase.

The SAD shown in figure 15(d) corresponds to a domain marked 'B'. The presence of superlattice spots along the  $[110]$ -type direction indicate the occurrence of the new superlattice phase, as discussed in section 3.4.2, in the oxygenated SCT40 as well. The new superlattice phase was observed in various grains of oxygenated SCT40.

In section 3.4.1 we observed that the *Pbcm* phase is present even up to room temperature in the un-oxygenated SCT40 sample whereas in oxygenated SCT40 no *Pbcm* phase was observed at room temperature. The  $\epsilon'-T$  data in figures 1(b) and (c) clearly indicate that for un-oxygenated SCT40 the first-order AFE phase transition is very broad, whereas for the oxygenated SCT40 the AFE phase transition is very sharp. Thus the observed broadening of the first-order AFE phase transition, due to oxygen deficiency, gets sharper on

oxygenation of SCT40. Thus the  $\epsilon'-T$  behavior and the TEM observations related to SCT40, are in complete accordance. In the un-oxygenated SCT40 sample the AFE *Pbcm* phase is present even at RT because the oxygen deficiency has basically broadened the AFE phase transition.

From the Curie–Weiss plot shown in the inset of figure 1(c) it is obvious that  $\epsilon'-T$  deviates from the Curie–Weiss behavior only below  $\sim 250$  K, i.e. the SCT40 is paraelectric at and above 250 K. In the light of this it is inferred that the weak superlattice peaks as indicated by arrows in the insets of XRD pattern in figure 2(b), basically correspond to the newly observed superlattice phase, which is paraelectric at room temperature. Since this new ordering is also a four-times modulation along  $[100]$  of the perovskite, the interplanar spacings corresponding to these superlattice peaks will be too

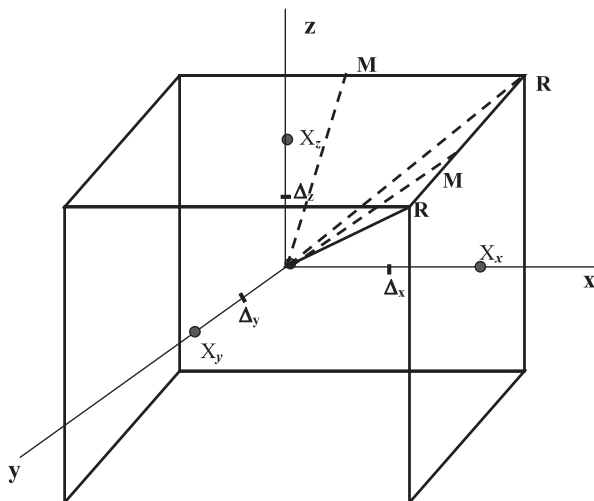


**Figure 16.** Sketch showing the equivalent  $\Delta$ -points ( $\Delta_x$ ,  $\Delta_y$ ,  $\Delta_z$ ) in the cubic Brillouin zone of the perovskite.

close to the superlattice peaks due to *Pbcm* ordering and hence will get fitted during a Rietveld refinement done using *Pbcm* space group. For SCT40 the PE to AFE phase transition takes place at  $\sim 230$  K only.

### 3.6. The origin and nature of the new superlattice ordering

After careful analysis of the two superlattice orderings observed in the SAD patterns of figures 6(a) and (b), figures 10(c) and (d) and 14(b), we find that these three type of ordering along  $[110]$ ,  $[\bar{1}10]$  and  $[001]$  of the  $P2_12_12/Pbnm$  phases are equivalent to four-times modulation of the basic perovskite cell along any of its  $[100]$ -type directions. This indicates that the  $\Delta$ -point instability is equally probable in all  $[100]$ -type directions. This is in complete accordance with the cubic symmetry of the basic perovskite structure. This can be realized from figure 16 showing the equivalent  $\Delta$ -points ( $\Delta_x$ ,  $\Delta_y$ ,  $\Delta_z$ ) in the BZ of the basic perovskite structure.

The temperature dependent microstructural changes related with the PE to AFE transformation and back to PE, shown in figure 7 are very interesting and pose some basic feature about the nature of the phase transition initiated by the  $\Delta$ -point instability. The randomness in the microstructural features, as shown in figures 5(b) and 7(b), (c) indicates that the selection of the nucleation points for the growth of AFE phase, is completely probabilistic. Although the orderings produce doubling of the cell parameters of the PE phase, the random nucleation and growth of the AFE domains is completely uncorrelated with the existing twin domains of the PE phase  $P2_12_12/Pbnm$  i.e. the occurrence of atomic displacements giving rise to the *Pbcm* phase have nothing to do with the pre-existing atomic arrangement of the PE  $P2_12_12/Pbnm$  phase. Since the conclusion regarding the correlation between the ordering directions of the final AFE phase and the parent phase has been drawn based purely on the powder diffraction data this important fact has remained invisible. It is on such occasions that the combined information on the microstructure and

corresponding diffraction, which is provided only by TEM studies, become unsurpassable by any other technique. Thus it is clear that the  $\Delta$ -point instability washes out all the domain boundaries of the  $P2_12_12$  phase existing prior to the phase transformation. It does not matter what state of antiferrodistortion exists in the  $P2_12_12$  orthorhombic phase. It originates as a result of energetics involving the octahedral distortion taking place in basic framework of the pseudoperovskite structure only. What is more interesting is the exact recovery of the twin band contrast after heating back to RT. This indicates some microstructural memory mechanism operating across the phase transition. Such memory effects have been found in other similar martensitic type phase transformations [14]. The reported memory mechanism [19–22] is based on the symmetry confirming property of the short-range order defects, which are quite probable in these compounds too.

## 4. Conclusion

Based on above described results of room-temperature and low-temperature structural studies, using XRD and TEM on oxygenated and un-oxygenated SCT30 and SCT40, it can be concluded that, together with the *Pbcm* phase, which is typified by the structural modulation originating from the  $\Delta$ -point instability along  $[001]$  of the  $P2_12_12$  (and *Pbnm*) phase, a new superlattice phase also exists. This appears across the antiferroelectric phase transition in SCT30 and remains in SCT40 at room temperature. This arises as a result of structural modulation along  $[110]$  and  $[\bar{1}10]$  of  $P2_12_12$  (or *Pbnm*) phase. This has been verified by the occurrence of two-dimensional lattice fringes of  $15.5 \text{ \AA} \times 15.5 \text{ \AA}$  periodicity. From the temperature dependent dielectric permittivity ( $\epsilon'-T$ ) variation of the oxygenated SCT40 sample it appears that this new phase is paraelectric at room temperature. This newly observed structural modulation also appears to be a result of  $\Delta$ -point instability only. It appears that the  $\Delta$ -point instability follows the cubic symmetry and is equally probable in all the three  $[100]$ -type directions of the BZ of the basic perovskite structure. Based on the comparative  $\epsilon'-T$  study on oxygenated and un-oxygenated SCT40 samples it is concluded that the oxygen deficiency induces broadening of the first-order antiferroelectric phase transition in SCT.

## References

- [1] Sharine G and Yamada Y 1969 *Phys. Rev.* **177** 858
- [2] Pytte E and Feder J 1969 *Phys. Rev.* **187** 1077
- [3] Zhong W, Vanderbilt D and Rabe K M 1994 *Phys. Rev. Lett.* **73** 1861
- [4] Bernorz J G and Muller K A 1984 *Phys. Rev. Lett.* **52** 2289
- [5] Minikiewicz V J and Shirane G 1968 *Bull. Am. Phys. Soc.* **13** 1376
- [6] Muller K A, Brun E, Derighetti B, Drumheller J E and Waldner F 1964 *Phys. Lett.* **9** 223
- [7] Anwar S and Lalla N P 2007 *J. Phys.: Condens. Matter* **19** 436210
- [8] Anwar S and Lalla N P 2008 *Solid State Sci.* **10** 307

- [9] Ranjan R, Pandey D and Lalla N P 2000 *Phys. Rev. Lett.* **84** 3726
- [10] Ranjan R and Pandey D 2001 *J. Phys.: Condens. Matter* **13** 4239–49  
Ranjan R and Pandey D 2001 *J. Phys.: Condens. Matter* **13** 4251–66
- [11] Cowley A C S, Lukaszewicz K and Megaw H D 1969 *Acta Crystallogr. B* **25** 851
- [12] Ranjan R, Pandey D, Schuddinck W, Richard O, Meulencere P D, Landuyt J V and Tandeloo G V 2001 *J. Solid State Chem.* **162** 20
- [13] Howard C J, Withers R L, Knight K S and Zhang Z 2008 *J. Phys.: Condens. Matter* **20** 135202
- [14] Anwar S and Lalla N P 2008 *J. Solid State Chem.* **181** 11
- [15] Jona F, Shirane G, Mazzi F and Pepinsky R 1957 *Phys. Rev.* **105** 849
- [16] Anwar S and Lalla N P 2008 *Appl. Phys. Lett.* **21** 212901
- [17] Mishra S K, Ranjan R, Pandey D and Stokes H T 2006 *J. Phys.: Condens. Matter* **18** 1885
- [18] Mishra S K, Ranjan R, Pandey D, Ranson P, Ouillon R, Lucarre J P and Pruzan P 2006 *J. Phys.: Condens. Matter* **18** 1899
- [19] Ren X and Otsuka K 2000 *Phys. Rev. Lett.* **85** 1016
- [20] Ren X and Otsuka K 1997 *Nature* **389** 579
- [21] Ren X 2004 *Nat. Mater.* **3** 91
- [22] Sun D, Ren X and Otsuka K 2005 *Appl. Phys. Lett.* **87** 142903